Chemistry–A European Journal
Research Article
doi.org/10.1002/chem.202401960
Chemistry Europe
European Chemical Societies Publishing
www.chemeurj.org

Three Perovskite Phases with Different Cation Orders in $Sm_2MnMn(Mn_{4-x}Sb_x)O_{12}$

Xuan Liang,[b, c] Kazunari Yamaura,[b, c] and Alexei A. Belik*[a]

Cation order, which can be controlled by synthesis conditions and stoichiometry, plays an important role in properties of perovskite materials. Here we show that aliovalent doping by Sb^{5+} in $Sm_2MnMn(Mn_{4-x}Sb_x)O_{12}$ quadruple perovskite solid solutions can control cation orders in both A and B sites. Samples with $0.4 \le x \le 2$ were synthesized by a high-pressure, high-temperature method at 6 GPa and 1770 K. Three regions with different cation orders were found at $0.5 \le x \le 1.0$, $x = 1.5$–1.6, and $x = 1.8$. The $0.5 \le x \le 1.0$ compositions have a B-site-disordered and A-site columnar-ordered structure with space group $P4_2/nmc$; the $x = 1.5$ and 1.6 samples have a B-site rock-salt-ordered and A-site columnar-ordered structure with space group $P4_2/n$; the $x = 1.8$ sample has a B-site rock-salt-ordered and A-site-disordered structure with space group $P2_1/n$. All the samples show one ferrimagnetic transition: T_C increases from 35 K to 73 K for $0.5 \le x \le 1.0$, $T_C = 81$ K for $x = 1.5$ and 1.6, and $T_C = 53$ K for $x = 1.8$.

Introduction

While the number of natural perovskite-type minerals is limited, synthetic ABO_3 perovskite-type oxides are numerous, and the perovskite structure is the most adaptive in inorganic chemistry. Perovskites are noteworthy in their ability to take a wide range of cations on the A and B sites resulting in a variety of practically important properties such as catalytic, ferroelectric, ferromagnetic, and superconductive.[1–4] Cations in both A and B sites of perovskite oxides can order in three types: layered, columnar, and rock-salt arrangements.[5,6] B-site orders in perovskites, driven by oxidation state differences, have most examples,[7,8] including double, triple, and quadruple perovskites, $A_2BB'O_6$, $A_3BB'_2O_9$, and $A_4BB'_3O_{12}$. Quadruple perovskites with $AA'_3B_4O_{12}$ and $A_2A'A''B_4O_{12}$ compositions are common in A-site-ordered structures while A-site-ordered $AA'B_2O_6$ double perovskites are much rarer and usually realized together with simultaneous 1:1 cation orders at both A and B sites; they are called doubly ordered (or double double) perovskites, $AA'BB'O_6$.[9] The A-site columnar-ordered quadruple perovskites, $A_2A'A''B_4O_{12}$, have an intrinsic triple 2:1:1 order of the 10-coordinated A site, 4-coordinated square-planar A′ site, and 4-coordinated tetrahedral A″ site, but if A′ and A″ cations are the same, the intrinsic triple order will be hidden.[10,11] They are formed through large octahedral tilts of the $a^+a^+c^-$ type in the Glazer notation.[12] Complex exchange interactions in such perovskites can produce different frustration networks and many unusual physical properties in comparison with other oxygen-stoichiometric perovskites because of the existence of the unique tetrahedral A″ positions.[11,13,14]

Properties of perovskite-type materials can be modified through cation order, which in turn can be controlled by different synthesis conditions and different stoichiometries especially utilizing differences in oxidation states, ionic radii, and electronic structures of cations.[5] For example, there is a dramatic switch of magnetic properties from ferromagnetic order with full magnetization of $5\mu_B$ in cation-ordered R_2NiMnO_6 (R = rare earth elements) to spin glass behaviour with noticeably reduced magnetization in cation-disordered R_2NiMnO_6.[15,16] In $LaBaMn_2O_6$ with colossal magnetoresistance, the Curie temperature increases from 270 K in a disordered phase to 335 K for a cation-ordered phase.[17] Some perovskites allow continuous transformations of cation-ordered and disordered phases under specific conditions, such as thermal transformations of $Ba(Zn_{1/3}Ta_{2/3})O_3$,[18] $CaMnMnWO_6$, $SmMnMnTaO_6$,[19] and $(NaY)MnMnTi_4O_{12}$.[20] Furthermore, a pressure-induced inverse order-disorder transition in Y_2CoIrO_6 and Y_2CoRuO_6 has been reported.[21]

In this work, we report composition-induced changes in cation orders through aliovalent doping by Sb^{5+} at the B sites of $Sm_2MnMn(Mn_{4-x}Sb_x)O_{12}$ solid solutions. By such doping at one site, we could control cation ordering at both A and B sites and could realise a transition from A-site-ordered/B-site-disordered to simultaneously A- and B-site-ordered and finally to A-site-disordered/B-site-ordered structures. To the best of our knowledge, such a transition was not realized before. The $x = 2$

[a] Dr. A. A. Belik
Research Center for Materials Nanoarchitectonics (MANA)
National Institute for Materials Science (NIMS)
Namiki 1–1, Tsukuba, Ibaraki 305-0044 (Japan)
E-mail: Alexei.Belik@nims.go.jp
[b] X. Liang, Dr. K. Yamaura
Research Center for Materials Nanoarchitectonics (MANA)
National Institute for Materials Science (NIMS)
Namiki 1–1, Tsukuba, Ibaraki 305-0044 (Japan)
[c] X. Liang, Dr. K. Yamaura
Graduate School of Chemical Sciences and Engineering
Hokkaido University
North 10 West 8, Kita-ku, Sapporo, Hokkaido 060-0810 (Japan)

Supporting information for this article is available on the WWW under https://doi.org/10.1002/chem.202401960

sample, prepared at 10 GPa, was previously reported to have an A-site-ordered/B-site-ordered structure, and it is located near the phase boundary as $Eu_2MnMn(Mn_2Sb_2)O_{12}$ (≡ $EuMn(MnSb)O_6$) was found in an A-site-disordered/B-site-ordered structure.[22]

Results and Discussion

The $x=0.4$ sample crystallized in space group $P4_2/nmc$ and contained about 8.1 wt.% of $SmMn_7O_{12}$ perovskite $AA'_3B_4O_{12}$-type impurity, while the $x=0.5$ sample contained only traces of $SmMn_7O_{12}$ impurity (1.2 wt.%, which could be determined only with high-quality synchrotron X-ray powder diffraction (XRPD)) (Figures S1a and S2). These results showed that the $Sm_2MnMn(Mn_{4-x}Sb_x)O_{12}$ solid solutions are formed from $x=0.5$, and we did not prepare samples with $x<0.4$ for this reason. We note that small amounts of a pyrochlore-type phase were observed in all samples (see, for example, Figure 1), but since it is not a perovskite-type phase we will not discuss it further. Samples with $0.5\leq x\leq 1.0$ adopted a tetragonal structure with space group $P4_2/nmc$ (No. 137), and their phase purity reached 98-99 %. The $x=1.1$ sample already contained about 6.6 wt.% of a phase with space group $P4_2/n$, as could be clearly seen from the appearance of a peak near 19.80° (for CuKα radiation), which originates from the B-site cation order of the $P4_2/n$ structure (Figure S1b); its Miller index is (111), and it is absent in the $P4_2/nmc$ structure. The amount of a $P4_2/n$ phase increased to 77% in the $x=1.4$ sample suggesting a two-phase region between the $x=1.1$ and 1.4 compositions.

Therefore, we did not prepare samples with $x=1.2$ and 1.3. Samples with $x=1.5$ and 1.6 adopted the tetragonal structure with space group $P4_2/n$ (No. 86), and their phase purity reached about 90 % – a characteristic reflection of the $P4_2/nmc$ structure near 33.2° (for CuKα radiation) disappeared in these samples (Figures S1d and S1f). The sample with $x=1.8$ crystallised in space group $P2_1/n$ (No. 14), and its phase purity was about 95 % – this structure has two characteristic reflections near 19.45° and 19.85° (for CuKα radiation), and the absence of any reflections near 16.05° (Figure S1e). Samples with $x=1.7$, 1.9, 2.0 were a mixture of $P4_2/n$ and $P2_1/n$ phases, and the $x=2.0$ sample additionally contained an unidentified impurity (all impurity peaks could be indexed in space group $R\bar{3}$ with $a=7.4299$ Å and $c=8.7800$ Å). The compositional dependence of lattice parameters obtained from synchrotron XRPD data is illustrated in Figure 2 (values are given in Table S1), where weight fractions are also given for samples containing several perovskite-type phases.

Experimental, calculated, and difference synchrotron XRPD patterns of all samples are shown in Figures S2-S4 and Figure 1 for the $x=1$ sample as an example. Refined structural parameters and bond lengths are summarized in Tables S2-S9. Structure parameters of $Sm_2MnMn(Mn_{4-x}Ti_x)O_{12}$, $Sm_2MnMn(Mn_2Sb_2)O_{12}$, and $EuMn(MnSb)O_6$ were used as initial models for the structure refinements of $Sm_2MnMn(Mn_{4-x}Sb_x)O_{12}$ with $0.5\leq x\leq 1.0$, $x=1.5$–1.6, and $x=1.8$, respectively.[22,23] It was found that the cations at the Mn1 square-planar site (A′) of all samples are disordered from the ideal 2*a* site (0.75, 0.25, 0.75) with the full occupation to a half-occupied 4*c* site (0.75, 0.25, *z*) (for the $P4_2/nmc$ model as an example). Refinements of occupation factors (*g*) showed that there were antisite disorders of Sm/Mn atoms between the A/A′ sites (samples with $0.5\leq x\leq 1.0$ and $x=1.5$–1.6) and the A/A″ sites (samples with $0.5\leq x\leq 1.0$ and $x=1.5$) (Figure 3c). However, the degree of antisite disorder was small. The presence of small amounts of heavier rare-earth elements at the square-planar A′ site and tetrahedral A″ site was also observed in other $A_2A'A''B_4O_{12}$-type compounds.[22–25] Different crystal structures observed in the $Sm_2MnMn(Mn_{4-x}Sb_x)O_{12}$ system are illustrated in Figure 4.

The formation of the $Sm_2MnMn(Mn_{4-x}Sb_x)O_{12}$ solid solutions (in a nearly single-phased form) is observed from $x=0.5$ when the concentration of Mn^{2+} reaches 18% and one A site (namely, tetrahedral A″ (or Mn2) site) can be fully occupied by Mn^{2+}: $Sm_2Mn^{3+}Mn^{2+}(Mn^{3+}{}_{3.5}Sb_{0.5})O_{12}$. It is consistent with crystallographic considerations because Mn^{3+} cations cannot be located in tetrahedral sites.[26] The Mn2–O bond lengths remain nearly constant in all samples because the Mn2 site is occupied by

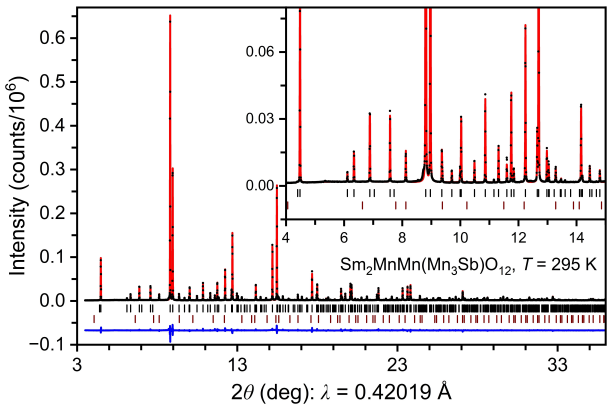

Figure 1. Fragments of experimental (black crosses), calculated (red line), and difference (blue line) synchrotron XRPD patterns of $Sm_2MnMn(Mn_{4-x}Sb_x)O_{12}$ with $x=1$ at $T=295$ K. The tick marks show possible Bragg reflection positions of the main perovskite phase (the first row) and pyrochlore impurity (the second row). The inset shows a zoomed fragment.

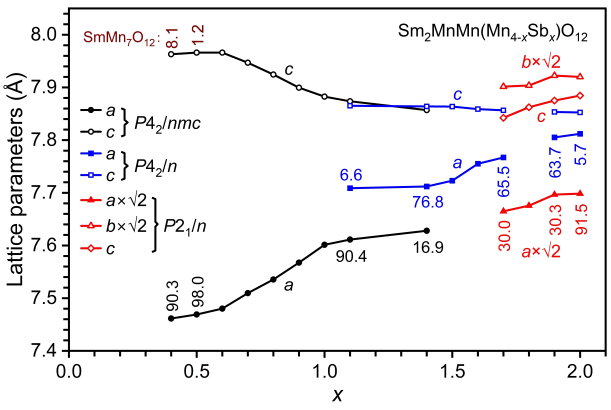

Figure 2. Compositional dependence of the lattice parameters in $Sm_2MnMn(Mn_{4-x}Sb_x)O_{12}$ solid solutions for $0.4\leq x\leq 2.0$ from synchrotron XRPD data at room temperature. Numbers show weight fractions (in %) of corresponding phases for multi-phased samples; see Tables S1–S9 for details.

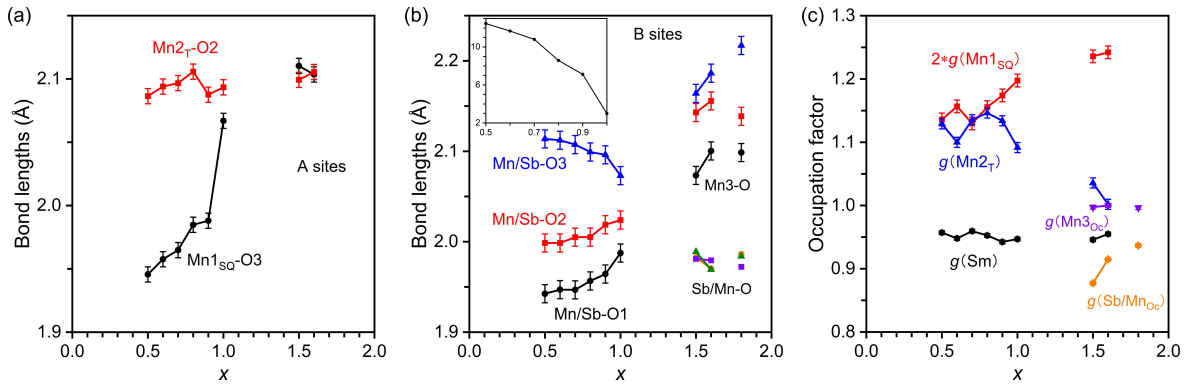

Figure 3. Compositional dependence of a) Mn1–O (square-planar, SQ) and Mn2–O (tetrahedral, T) bond lengths, b) Mn/Sb–O, Mn3–O, and Sb/Mn–O (octahedral, Oc) bond lengths; the inset shows the octahedral distortion parameter ($\times 10^4$), and c) cation occupation factors in $Sm_2MnMn(Mn_{4-x}Sb_x)O_{12}$ solid solutions for $x = 0.5 \leq x \leq 1.0$, 1.5, 1.6, and 1.8 from synchrotron XRPD data at room temperature. Only Mn was assumed at the Mn1, Mn2, and Mn3 (or Mn in $P2_1/n$) sites, only Sm was assumed at the Sm site, and only Sb was assumed at the Sb/Mn site on panel (c).

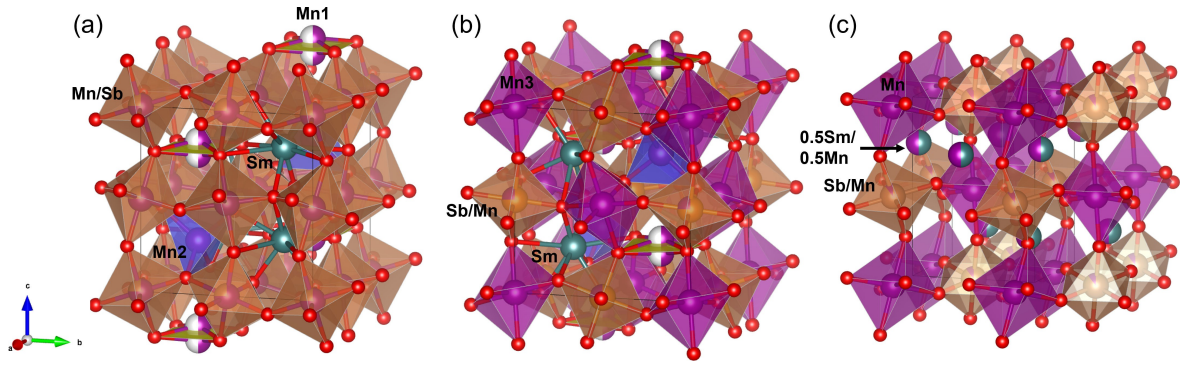

Figure 4. Fragments of crystal structures of $Sm_2MnMn(Mn_{4-x}Sb_x)O_{12}$ with different space groups in a polyhedral presentation. a) $P4_2/nmc$, b) $P4_2/n$, and c) $P2_1/n$. $Mn1O_4$ square-planar (yellow), $Mn2O_4$ tetrahedra (blue), $(Mn/Sb)O_6$ or $(Sb/Mn)O_6$ octahedra (orange), and $Mn3O_6$ or MnO_6 octahedra (purple) are shown.

Mn^{2+} (Figure 3a). On the other hand, the Mn1–O bond lengths increase with increasing x corresponding to the change in the Mn oxidation state from +3 ($x = 0.5$) to +2 ($x = 1$: $Sm_2Mn^{2+}Mn^{2+}(Mn^{3+}{}_3Sb)O_{12}$). One octahedral Mn/Sb site in $Sm_2MnMn(Mn_{4-x}Sb_x)O_{12}$ with $0.5 \leq x \leq 1.0$ shows quite strong Jahn-Teller distortion, and the octahedral distortion parameter monotonically decreases with increasing x consistent with decreasing amount of Mn^{3+} cations (Figure 3b). The structural analysis of the samples with the B-site-ordered structures showed that one B site (Mn3 in $P4_2/n$ or Mn in $P2_1/n$) is always occupied by Mn, while the second B′ site (called Sb/Mn) has a mixture of Sb and Mn (Figure 3c).

Our synthesis at 6 GPa gave some amount of an unidentified impurity in the $x = 2$ sample. Therefore, 6 GPa could not be high enough to stabilize the $x = 2$ sample. In addition, the previous work showed that at the 10 GPa synthesis pressure, the phase boundary is located between Sm and Eu for $x = 2$, that is, $Sm_2MnMn(Mn_2Sb_2)O_{12}$ crystallizes in space group $P4_2/n$, while $EuMn(MnSb)O_6$ – in space group $P2_1/n$.[22] A lower pressure of 6 GPa could shift the phase boundary, and the Sm-containing samples, $Sm_2MnMn(Mn_{4-x}Sb_x)O_{12}$, could be exactly at the phase boundary. Therefore, an additional variable parameter (the composition x) could easily move the system between different phases in the vicinity of $x = 2$. This is why we obtained the $P4_2/n$ phase for $x = 1.5$ and 1.6, the $P2_1/n$ phase for $x = 1.8$, and mixtures of the $P4_2/n$ and $P2_1/n$ phases for $x = 1.7$, 1.9, and 2.0.

Magnetic properties of $Sm_2MnMn(Mn_{4-x}Sb_x)O_{12}$ with $0.5 \leq x \leq 1.0$, $x = 1.5$–1.6 and $x = 1.8$ under applied magnetic fields of 100 Oe and 10 kOe were measured. As shown in Figure 5a, the magnetic susceptibility curves, χ versus T ($\chi = M/H$), of $Sm_2MnMn(Mn_{4-x}Sb_x)O_{12}$ with $x = 1.0$ demonstrated a significant divergence between the 100 Oe ZFC and FCC curves (ZFC: zero-field-cooled, FCC: field-cooled on cooling) with characteristic broad maxima on the 100 Oe ZFC curves and a sharp monotonic rise of magnetic susceptibilities below $T_C = 73$ K, where the ferrimagnetic Curie temperature, T_C, was defined from a sharp peak on the differential curve, 100 Oe FCC $d\chi T/dT$ versus T. These behaviours indicated the development of large uncompensated magnetic moments. The χ versus T curves of other samples are illustrated in Figures S5–S7. The negative Curie-Weiss temperatures, obtained by fitting the inverse 10 kOe FCC magnetic susceptibility curves (χ^{-1} versus T) between 200 K and 395 K, indicate predominantly antiferromagnetic interactions in all samples (Table 1). The experimental effective magnetic moments were close to the expected ones (in calculations we used 1.5 μ_B for Sm^{3+}).[27] The FCC curves under 100 Oe of the multi-phased $Sm_2MnMn(Mn_{4-x}Sb_x)O_{12}$ samples

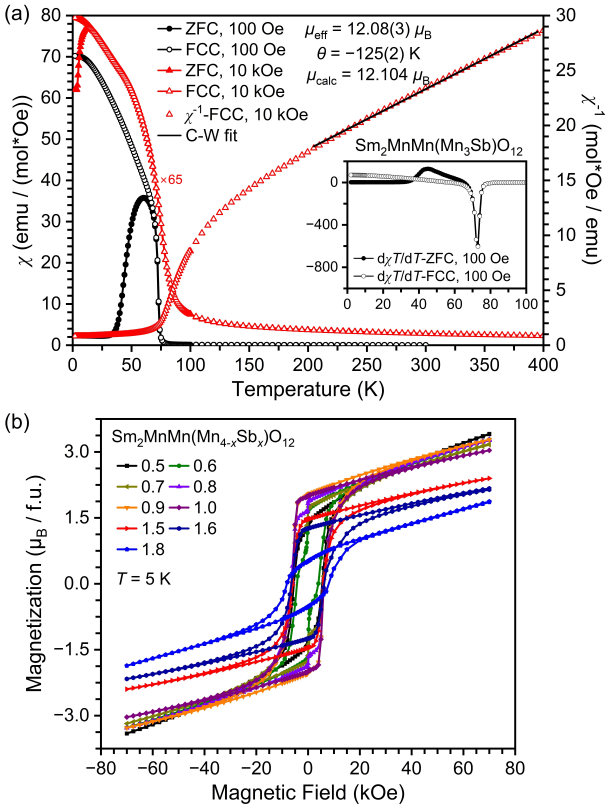

Figure 5. a) ZFC (filled symbols) and FCC (empty symbols) dc magnetic susceptibility ($\chi = M/H$) curves of $Sm_2MnMn(Mn_{4-x}Sb_x)O_{12}$ with $x = 1.0$ measured at 100 Oe (black, circles) and 10 kOe (red, triangles). The black line gives the Curie–Weiss fit (C–W fit) for the FCC χ^{-1} versus T curve at 10 kOe (the right-hand axis). The inset shows 100 Oe ZFC and FCC $d\chi T/dT$ versus T curves. b) M versus H curves of $Sm_2MnMn(Mn_{4-x}Sb_x)O_{12}$ with $x = 0.5 \leq x \leq 1.0$, 1.5, 1.6, and 1.8 at 5 K.

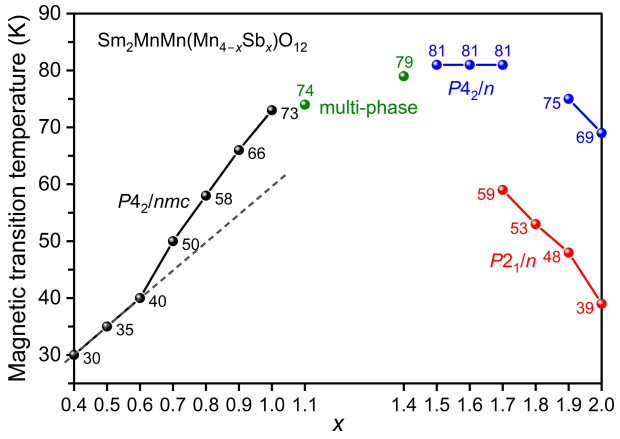

Figure 6. The ferrimagnetic Curie temperature (T_C) of $Sm_2MnMn(Mn_{4-x}Sb_x)O_{12}$ with $0.4 \leq x \leq 1.1$ and $1.4 \leq x \leq 2.0$. Numbers show the T_C values in K.

with $x = 0.4$, 1.1, 1.4, 1.7, 1.9, and 2.0 were also measured to determine their T_C (Figures S8–S11). Two-phase samples with $x = 0.4$, 1.7, 1.9, and 2.0 showed two significant magnetic transitions, while samples with $x = 1.1$ and 1.4 showed only one transition from the majority phase. The composition dependence of T_C is shown in Figure 6. With the increase of x from 0.4 to 1.0 (within space group $P4_2/nmc$), T_C exhibited two approximately linearly increasing trends. It is unusual that T_C increases with increasing the amount of non-magnetic Sb^{5+} cations. On the other hand, the amount of Mn^{2+} cations also increases with increasing x. The presence of isotropic Mn^{2+} with larger spin ($S = 5/2$) in comparison with Mn^{3+} ($S = 2$) can enhance magnetic interactions and increase T_C. Samples with $x = 1.5$, 1.6, and 1.7 (for the $P4_2/n$ phase) showed almost constant $T_C = 81$ K. T_C increases just slightly on moving from the B-site-disordered structure to the B-site-ordered structure. On the other hand, T_C dropped to 53 K for $x = 1.8$, when A-site ordering is lost. Magnetic anomalies from the A-site-disordered $P2_1/n$ phase could be detected for $x = 1.7$, 1.8, 1.9, and 2.0, and T_C showed a monotonic decrease with increasing x as expected because of the increasing amount of the non-magnetic dopant.

Isothermal magnetization curves (M versus H) of all samples at 5 K (Figure 5b) show similar well-defined hysteresis with large remnant magnetization (M_R) and coercive field of about 4-8 kOe (Table 1). On the other hand, no hysteresis was observed at 100 K as 100 K is higher than the T_C of all samples (Figures S12–S14). The observed M versus H curves are typical for ferrimagnets. Specific heat data at $H = 0$ and 90 kOe are given in Figures S15-S17. Characteristic λ-type peaks near T_C were observed in all samples, confirming a long-range magnetic

Table 1. Temperatures of magnetic anomalies and parameters of Curie-Weiss fits and M versus H curves at $T = 5$ K for $Sm_2MnMn(Mn_{4-x}Sb_x)O_{12}$ with $x = 0.5 \leq x \leq 1.0$, 1.5, 1.6, and 1.8.

x	T_C (K)	μ_{eff} (μ_B/f.u.)	μ_{calc} (μ_B/f.u.)	θ (K)	M_S (μ_B/f.u.)	M_R (μ_B/f.u.)	H_C (kOe)
0.5	35	11.91(3)	12.145	−114(2)	3.411	1.355	4.00
0.6	40	11.84(2)	12.137	−113.9(11)	3.276	1.616	5.46
0.7	50	12.08(3)	12.128	−127(2)	3.180	1.678	5.82
0.8	58	12.00(2)	12.120	−114(2)	3.265	1.830	6.19
0.9	66	12.29(2)	12.112	−119.0(12)	3.280	2.029	6.23
1.0	73	12.08(3)	12.104	−125(2)	3.036	2.000	6.15
1.5	81	12.06(2)	12.062	−110.2(12)	2.399	1.467	5.86
1.6	81	12.23(1)	12.054	−115.1(7)	2.164	1.263	6.20
1.8	53	12.14(2)	12.037	−102.5(13)	1.859	0.518	7.98

ordering and also confirming that the observed magnetic-susceptibility anomalies originate from the main phases (not from impurities) as small amounts of impurities cannot give large specific heat anomalies (as this method probes bulk properties). In addition, pyrochlore-type phases in these systems show only spin-glass behavior below about 5 K[28] and cannot be responsible for the observed strong anomalies near T_C, and neutron diffraction studies of the $x=2$ samples confirmed long-range ferrimagnetic structures.[22]

Conclusions

In conclusion, we demonstrated that cation orders in *both* A and B sites could be controlled in the $Sm_2MnMn(Mn_{4-x}Sb_x)O_{12}$ solid solutions via aliovalent doping by Sb^{5+} only at the B site. $Sm_2MnMn(Mn_{4-x}Sb_x)O_{12}$ is a unique system as it is located close to a phase boundary resulting in the appearance of three perovskite phases as a function of the composition. All the samples show one ferrimagnetic transition with systematic changes in the ferrimagnetic Curie temperature.

Supporting Information

Supporting information (SI) is available which contains experimental details and additional Figures and Tables as described throughout the text. The authors have cited additional references within the Supporting Information.[29–31]

Acknowledgements

This work was partially supported by a Grant-in-Aid for Scientific Research (No. JP22H04601) from the Japan Society for the Promotion of Science and the Kazuchika Okura Memorial Foundation (No. 2022-11). Synchrotron radiation was used at the powder diffraction beamline BL02B2 at SPring-8, with permission from the Japan Synchrotron Radiation Research Institute (Proposal Numbers: 2023A1496 and 2023B1676). MANA is supported by the World Premier International Research Center Initiative (WPI), MEXT, Japan.

Conflict of Interests

The authors declare no conflict of interest.

Data Availability Statement

The data that support the findings of this study are available from the corresponding author upon reasonable request.

Keywords: A-site columnar-ordered · antisite disorder · double perovskites · ferrimagnet · quadruple perovskites

[1] J. G. Bednorz, K. A. Müller, *Rev. Mod. Phys.* **1988**, *60*, 585–600.
[2] A. S. Bhalla, R. Guo, R. Roy, *Mater. Res. Innovations* **2000**, *4*, 3–26.
[3] N. Nuraje, K. Su, *Nanoscale* **2013**, *5*, 8752–8780.
[4] K. Hirose, R. Sinmyo, J. Hernlund, *Science* **2017**, *358*, 734–738.
[5] A. M. Abakumov, A. A. Tsirlin, E. V. Antipov, in *Comprehensive Inorganic Chemistry II (Second Edition)* (Eds.: J. Reedijk, K. Poeppelmeier), Elsevier, Amsterdam, **2013**, pp. 1–40.
[6] G. King, P. M. Woodward, *J. Mater. Chem.* **2010**, *20*, 5785–5796.
[7] S. Vasala, M. Karppinen, *Prog. Solid State Chem.* **2015**, *43*, 1–36.
[8] A. Hossain, P. Bandyopadhyay, S. Roy, *J. Alloys Compd.* **2018**, *740*, 414–427.
[9] M. C. Knapp, P. M. Woodward, *J. Solid State Chem.* **2006**, *179*, 1076–1085.
[10] A. A. Belik, D. D. Khalyavin, L. Zhang, Y. Matsushita, Y. Katsuya, M. Tanaka, R. D. Johnson, K. Yamaura, *ChemPhysChem* **2018**, *19*, 2449–2452.
[11] A. A. Belik, *Dalton Trans.* **2018**, *47*, 3209–3217.
[12] A. M. Glazer, *Acta Crystallogr. Sect. B* **1972**, *28*, 3384–3392.
[13] K. Ji, R. Chen, P. Manuel, J. P. Attfield, *Z. Anorg. Allg. Chem.* **2023**, *649*, e202300047.
[14] A. M. Vibhakar, D. D. Khalyavin, P. Manuel, J. Liu, A. A. Belik, R. D. Johnson, *Phys. Rev. Lett.* **2020**, *124*, 127201.
[15] R. J. Booth, R. Fillman, H. Whitaker, A. Nag, R. M. Tiwari, K. V. Ramanujachary, J. Gopalakrishnan, S. E. Lofland, *Mater. Res. Bull.* **2009**, *44*, 1559–1564.
[16] M. Nasir, S. Kumar, N. Patra, D. Bhattacharya, S. N. Jha, D. R. Basaula, S. Bhatt, M. Khan, S.-W. Liu, S. Biring, S. Sen, *ACS Appl. Electron. Mater.* **2019**, *1*, 141–153.
[17] F. Millange, V. Caignaert, B. Domengès, B. Raveau, E. Suard, *Chem. Mater.* **1998**, *10*, 1974–1983.
[18] I. M. Reaney, I. Qazi, W. E. Lee, *J. Appl. Phys.* **2000**, *88*, 6708–6714.
[19] K. Ji, K. N. Alharbi, E. Solana-Madruga, G. T. Moyo, C. Ritter, J. P. Attfield, *Angew. Chem. Int. Ed.* **2021**, *60*, 22248–22252.
[20] R. Scatena, R. Liu, V. V. Shvartsman, D. D. Khalyavin, Y. Inaguma, K. Yamaura, A. A. Belik, R. D. Johnson, *Angew. Chem. Int. Ed.* **2023**, *62*, e202305994.
[21] Z. Deng, C. J. Kang, M. Croft, W. Li, X. Shen, J. Zhao, R. Yu, C. Jin, G. Kotliar, S. Liu, T. A. Tyson, R. Tappero, M. Greenblatt, *Angew. Chem. Int. Ed.* **2020**, *59*, 8240–8246.
[22] E. Solana-Madruga, A. M. Arevalo-Lopez, A. J. Dos Santos-Garcia, E. Urones-Garrote, D. Avila-Brande, R. Saez-Puche, J. P. Attfield, *Angew. Chem. Int. Ed.* **2016**, *55*, 9340–9344.
[23] A. A. Belik, L. Zhang, R. Liu, D. D. Khalyavin, Y. Katsuya, M. Tanaka, K. Yamaura, *Inorg. Chem.* **2019**, *58*, 3492–3501.
[24] A. A. Belik, R. Liu, K. Yamaura, *Ceram. Int.* **2023**, *49*, 14327–14334.
[25] R. Liu, M. Tanaka, H. Mori, Y. Inaguma, K. Yamaura, A. A. Belik, *J. Mater. Chem. C* **2021**, *9*, 947–956.
[26] D. Waroquiers, X. Gonze, G.-M. Rignanese, C. Welker-Nieuwoudt, F. Rosowski, M. Göbel, S. Schenk, P. Degelmann, R. André, R. Glaum, G. Hautier, *Chem. Mater.* **2017**, *29*, 8346–8360.
[27] C. Kittel, *Introduction to Solid State Physics*, John Wiley & Sons, Inc: New York, New York, **2005**.
[28] E. Solana-Madruga, A. J. Dos Santos-Garcia, C. Ritter, A. M. Arevalo-Lopez, D. Avila-Brande, E. Urones-Garrote, R. Saez-Puche, *Solid State Sci.* **2024**, *150*, 107499.
[29] S. Kawaguchi, M. Takemoto, K. Osaka, E. Nishibori, C. Moriyoshi, Y. Kubota, Y. Kuroiwa, K. Sugimoto, *Rev. Sci. Instrum.* **2017**, *88*, 085111.
[30] F. Izumi, T. Ikeda, *Mater. Sci. Forum* **2000**, *321–324*, 198–205.
[31] N. E. Brese, M. O'Keeffe, *Acta Crystallogr. Sect. B* **1991**, *47*, 192–197.

Manuscript received: May 20, 2024
Accepted manuscript online: May 22, 2024
Version of record online: July 1, 2024